

Localized Nanoresonator Mode in Plasmonic Microcavities

A. Casalis de Pury,^{1,2} X. Zheng,³ O. S. Ojambati,¹ A. Trifonov,⁴ C. Grosse,¹
 M.-E. Kleemann,¹ V. Babenko[Ⓞ],² D. Purdie,² T. Taniguchi,⁵ K. Watanabe,⁵ A. Lombardo,²
 G. A. E. Vandenbosch,³ S. Hofmann[Ⓞ],² and J. J. Baumberg[Ⓞ]^{1,*}
¹*Nanophotonics Centre, Cavendish Laboratory, University of Cambridge,
 JJ Thompson Avenue, Cambridge CB3 0HE, United Kingdom*
²*Cambridge Graphene Centre and Department of Engineering, University of Cambridge,
 9 JJ Thompson Avenue, Cambridge CB3 0FA, United Kingdom*
³*ESAT-TELEMIC, KU Leuven, B-300 Leuven, Belgium*
⁴*Spin Optics Lab, Saint Petersburg State University, Saint Petersburg 198504, Russia*
⁵*National Institute for Materials Science, 1-1 Namiki, Tsukuba 305-44, Japan*

 (Received 3 May 2019; revised manuscript received 29 January 2020; accepted 30 January 2020; published 6 March 2020)

Submicron-thick hexagonal boron nitride crystals embedded in noble metals form planar Fabry-Perot half-microcavities. Depositing Au nanoparticles on top of these microcavities forms previously unidentified angle- and polarization-sensitive nanoresonator modes that are tightly laterally confined by the nanoparticle. Comparing dark-field scattering with reflection spectroscopies shows plasmonic and Fabry-Perot-like enhancements magnify subtle interference contributions, which lead to unexpected redshifts in the dark-field spectra, explained by the presence of these new modes.

DOI: [10.1103/PhysRevLett.124.093901](https://doi.org/10.1103/PhysRevLett.124.093901)

Transparent dielectric materials are employed in diverse micro-optical resonators, ranging from semiconductor heterostructures to van der Waals materials [1–7]. More recently, there has been interest in utilizing high-bandgap materials as part of optoelectronic devices, such as hexagonal boron nitride (hBN), as well as active 2D semiconductors for low-energy switching, such as transition metal dichalcogenides (TMDs) [7–12]. Combining plasmonic metals with such microresonators introduces rich nano-optics [13–28]. Despite its simplicity and in clear contrast to previous results from related structures [29–32], we find plasmonic scattering processes from Au nanoparticles on submicron-thick dielectric layers are nontrivial, resulting in two distinct possible sets of nanocavity-nanoparticle modes depending on polarization and incidence angle. We identify a new mode that, rather than resulting from coupling of Fabry-Perot modes with localized plasmon resonances [27,28], requires angled transverse magnetic (TM) illumination and operates via a different Brewster mode mechanism. For submicron-thick dielectric layers, this mode is clearly identified and can be stronger than plasmon-coupled Fabry-Perot modes. The mode is characterized by a nanoscale-confined field that propagates beneath the nanoparticle.

Ultraflat planar microcavities here are formed from high-quality hBN crystals embedded into gold, formed by template exfoliation (Fig. 1; method in the Supplemental Material [33]). Each atomically flat terrace corresponds to a microcavity of different thickness with simple fabrication giving hundreds of ultraflat planar cavities distributed over centimeter-scale areas. Monodisperse and near-spherical

colloidal Au nanoparticles of 60 nm average diameter are then deposited from solution [38]. While our observations apply to all microcavities, hBN is helpfully inert, flat, insulating, chemically robust, and lacks exciton resonances that complicate these observations. The resultant samples are broadband illuminated through an objective with numerical aperture NA 0.8, so that light is collected for both dark-field (DF) and bright-field (BF) illumination in the angular range 0°–53° [Fig. 1(a)]. In BF, the angles of incidence and reflection are equal, while the average DF illumination angle is 58°. Microscope 100× images of a nanoparticle-on-microcavity (NPoMC) sample in BF [Fig. 1(b)] and DF [Fig. 1(c)] resolve individual Au nanoparticles in DF as orange spots on terrace 1 (T_1) and green spots on terrace 2 (T_2). More than 16 nanoparticles (NPs) are analyzed on each terrace displaying consistent spectra (see Supplemental Material [33], Fig. 2), while brighter (by $>3\sigma$) Au NP clusters are excluded, as are NPs near terrace edges.

The observed BF colors result from thin-film interference, which is used to calibrate each terrace thickness from the characteristic Fabry-Perot fringes [Fig. 2(a)], using uniaxial refractive indices $n_{x,y} = 1.65$, $n_z = 2.13$ (parallel to the c axis) [39]. Fitted spectra (dashed) generated by the same generalized Mie solver used to calculate DF scattering (see below), use reflectivities measured from the evaporated Au outside each hBN flake and give thicknesses $L_1 = 672 \pm 10$ nm for T_1 and $L_2 = 577 \pm 8$ nm for T_2 . Minor deviations in fringe amplitude are likely due to differences in Au roughness under and beside each hBN flake.

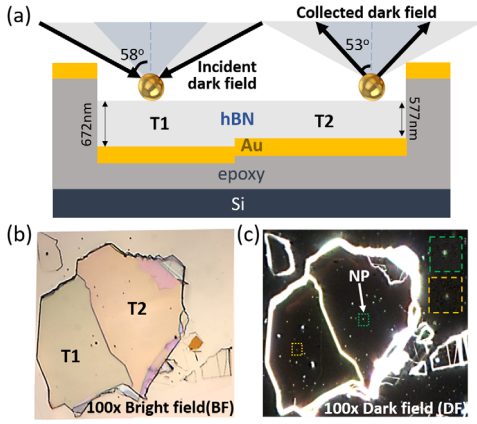


FIG. 1. Embedded hBN sample $\sim 60 \mu\text{m}$ wide, with two crystal terraces ($T1$, $T2$). (a) Cross section after nanoparticle deposition, showing in- and out-coupling angles for illumination with 0.8 NA objective. (b) Bright- and (c) dark-field images at 100 \times magnification showing individual nanoparticles on each terrace.

Dark-field scattering spectra collected from each terrace show intense distinct peaks similar for each nanoparticle [Fig. 2(b)]. Solid lines show the average over 22 ($T1$) and 16 ($T2$) nanoparticles (dashed lines show standard error). While the scattering efficiency of coupled 60 nm Au NPs on bare Si is $<0.2\%$, resonant enhancement here increases the scattered intensity by $\times 18$ ($T1$) and $\times 28$ ($T2$) [Fig. 2(b)]. This combination of high intensity and low variability enables reliable identification of features in the spectra, such as asymmetric line shapes and overlapping modes. In particular, we note that the scattering peaks are not at the expected positions (dashed lines) from the scattering interference paths depicted in Fig. 2(c) and that these peak shifts differ significantly between the two terraces.

Initially, two pathways are considered, interfering with the direct backscattering from the NP with the forward-scattered light after it has propagated multiple times through the underlying microcavity. The phase shift on reflection at the lower hBN-Au interface is $\pi + \delta(E, \theta)$. Dips in BF reflectivity correspond to microcavity resonances, where the resonant optical field inside the hBN increases light absorption in the Au mirror. In this situation, the optical field at the top surface is also maximized, so forward scattering from the NP is expected to be strongest at these reflectivity dips (for the same illumination angle). Since DF illumination is recorded at higher incident angles than the BF reflectivity, the cavity resonances blueshift [6,7,39] and for 58° are shown by the vertical dashed lines [Fig. 2(b)]. However, this model cannot account for the shifted DF scattering peaks [blue-green arrows, Fig. 2(b)]. All scattering peaks from both terraces are redshifted by different energies from the expected positions based on the simple model above, up to 300 meV for the higher energy $T2$ mode. This suggests that scattering resonances of nanoparticles on microcavities are influenced by extra

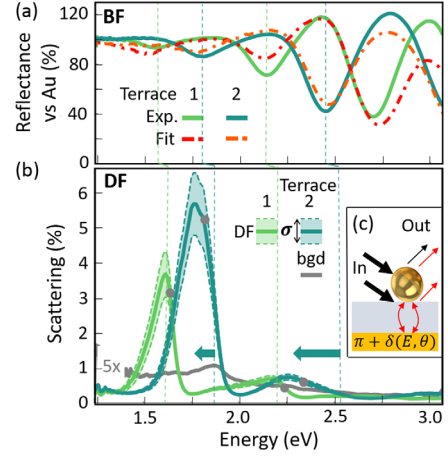


FIG. 2. (a) Bright-field reflectance and (b) dark-field scattering from 22 ($T1$) and 16 ($T2$) nanoparticles. Dashed lines show one standard error bound, gray line is scattering background ($\times 5$) from lower hBN-Au interface away from NPs, gray dots mark peak positions of Fano resonances from resulting interference. Vertical lines show expected TE-polarized wavelengths for $L_{1,2}$. (c) Schematic interference in scattering.

mechanisms besides the out-coupling of planar Fabry-Perot modes.

To better understand the resonant modes in this system, we calculate the extinction spectra without the NP and scattering spectra with the NP (Fig. 3). These are evaluated using a generalized Mie theory (see Supplemental Material [33]), considering a perfectly spherical Au nanoparticle on top of a uniform hBN layer on flat Au [Fig. 2(c)], with the z axis parallel to the optic axis of the hBN crystal. Initially, the fraction of light entering the hBN is calculated as the incident angle increases. Without the nanoparticle, the interface reflection matrix \mathbf{R} , which relates the reflected electric field \mathbf{E}_r to the incident field \mathbf{E}_i with incident s (E_{is}) and p polarization (E_{ip}) via

$$\mathbf{E}_r = \mathbf{R}\mathbf{E}_i = \begin{bmatrix} E_{rp} \\ E_{rs} \end{bmatrix} = \begin{bmatrix} R_{pp} & R_{ps} \\ R_{sp} & R_{ss} \end{bmatrix} \begin{bmatrix} E_{ip} \\ E_{is} \end{bmatrix} \quad (1)$$

is diagonal ($R_{ps} = R_{sp} = 0$), leaving only $R_{pp} = R_{\text{TM}}$ and $R_{ss} = R_{\text{TE}}$. Defining incident and reflected electric fields in terms of polarization-dependent refractive indices and incident angle θ_i , the overall TM reflection coefficient r_{TM} is described by [6,40]

$$r_{\text{TM}} = \frac{n_{xy}n_z \cos(\theta_i) - [n_z^2 - \sin^2(\theta_i)]^{1/2}}{n_{xy}n_z \cos(\theta_i) + [n_z^2 - \sin^2(\theta_i)]^{1/2}} \quad (2)$$

(assuming air above) and similar for TE. The TE reflection resonances are equally spaced at normal incidence and blueshift together with angle [Fig. 3(a)]. For TM reflectivity [Fig. 3(b)], this picture is complicated by effects at Brewster's angle (white dashed lines in Fig. 3), where the

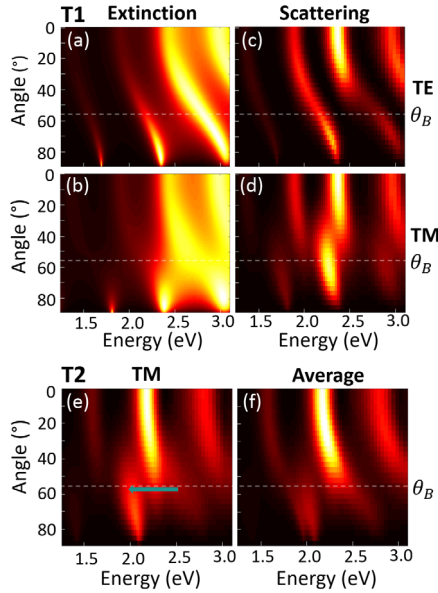


FIG. 3. Generalized Mie calculations for $T1$ (a)–(d) and $T2$ (e),(f). For $T1$, extinction without NP (a),(b) and scattering spectra for NP-on-microcavity (c),(d) are shown as angle increases. Brewster angle θ_B is dashed. Extinction is from 0% (black) to 100% (white), scattering from 0% (black) to 5% (white). For $T2$, calculations are for (e) TM scattering and (f) average of TE and TM scattering. Grey arrow is comparison with Fig. 2.

reflection at the air-hBN surface vanishes, eliminating multiple interference. Beyond this angle,

$$\theta_B = \text{asin} \left(\left[\frac{n_{xy}^2 - 1}{n_{xy}^2 - n_z^{-2}} \right]^{1/2} \right) \simeq 56^\circ, \quad (3)$$

the phase on reflection reverses, shifting the resonances by half their spacing.

This generalized Mie model shows that scattering from the NP atop the microcavity is indeed enhanced at each extinction maxima [Fig. 3(c) and 3(d)]. TE scattering peaks blueshift with angles matching the reflectivity dips, weakening slightly at θ_B when polarization-flipped NP scattering disappears. The predicted TE scattering peaks at 58° match the observed peaks at 2.25 and 1.55 eV [Fig. 3(b)] to within 0.1 eV. The larger extinctions at higher energy come from the stronger interband Au absorption above 2.5 eV.

By contrast, a completely different predicted behavior is seen for TM-polarized scattering [Fig. 3(d)]. Although blueshifts are initially seen, a set of new modes appears around θ_B , which dominate the total (TE + TM) scattering at 58° . Since scattering measurements are typically taken at high angles $\sim \theta_B$, it is vital to understand the origin of these NPoMC modes.

Comparing TM extinction [Fig. 3(b)] to scattering [Fig. 3(d)] highlights these peculiarities. At θ_B , the extinction shows no microcavity modes, however, the scattering spectrum gives new sharp modes. In simulations of the

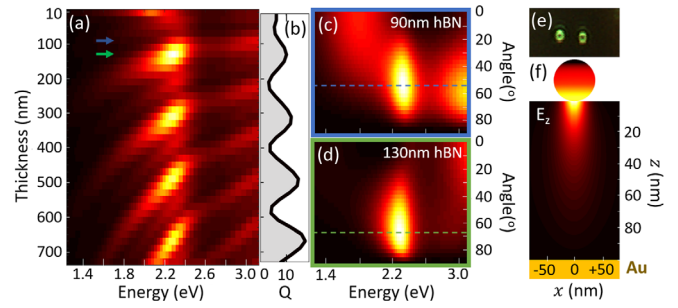


FIG. 4. (a) Thickness dependence of TM scattering of nanostructure modes at $\theta_i = \theta_B = 58^\circ$ and (b) Q factors. Arrows mark $L = 90, 130$ nm for angle dependences in (c),(d) where dashed lines mark angle of maximum scattering. (e) Typical experimental DF scattering images of ~ 100 -nm-thick hBN nanostructure at $100\times$ magnification. (f) Field map of surface charges on outside of 60 nm nanoparticle and scattered electric field (E_z) inside hBN for nanostructure mode with $L = 110$ nm, $\theta_i = 58^\circ$.

thinner microcavity $T2$ [Figs. 3(d) and 3(f)], the new peak at 1.9 eV becomes the dominant cavity mode, with a 200 meV redshift from the expected position of the TE scattering peak [Fig. 3(e), blue-green arrow]. This combination of nanostructure and Fabry-Perot modes accounts well for the bright mode near 1.8 eV in Fig. 2(b).

The theory shows these modes are produced by back-scattering from the NP, creating transverse localized cavity modes underneath it, which are spatially confined in plane to the nanoscale geometry of the NP (Fig. 4). Even for illumination angles significantly less than θ_B , these surface modes can be excited and out-coupled. This new nanostructure mode (NRM) is only seen at energies that can excite the microcavity-coupled vertical dipole antenna, forming a new scattering resonance at 2.25 eV.

To explore the nanostructure modes, we track how they vary with increasing microcavity thickness [Fig. 4(a)] [6,7,40]. The NRMs redshift with increasing hBN thickness for constant illumination angle of 58° . Above $L = 300$ nm, several modes are seen, with energy spacings that decrease as expected for Fabry-Perot-type modes. Between the strongly excited NRMs are weaker resonances matching the normal TE microcavity modes. Plotting the thickness-dependent Q factor of the dispersive NRMs shows a periodic modulation under an increasing envelope [Fig. 4(b)].

These resonant modes can be excited at incident angles from 40° – 80° with energies from 1.4–2.4 eV. The high-angle resonant lowest mode is clearly visible for hBN $L > 90$ nm [Figs. 4(c) and 4(d)]. They appear strongest when near resonant with the nanoparticle transverse plasmon mode around $\lambda = 550$ nm. The angle of maximum scattering intensity (blue and green lines, Figs. 4(c) and 4(d)) shifts from 52° to 68° when the hBN thickness increases from 90 to 130 nm, showing their coupling is not precisely tied to θ_B .

At thicknesses of 80–170 nm, the lowest NRM has the least extra contribution from the FP-coupled modes [Fig. 4(a)]. Experimentally, nanoparticles on hBN flakes within this range display ring-shaped dark-field scattering images due to the high-angle out-coupling of light from the NRMs [Fig. 4(e)]. This confirms their dominant out-of-plane E_z resonant fields, completely different from Fabry-Perot microcavities. These TM nanoresonator modes seen in the NPoMC geometry are thus attributed to multiple scattering and reflection underneath the NP [Fig. 4(f)]. This is because at θ_B all other cavity feedback disappears at the hBN-air interface. Treating scattering from the nanoparticle as a microcavity end mirror with low reflectivity (following Fabry-Perot behavior), we indeed expect the Q factor to increase with thickness. Such nanoresonators approach the limiting case when the lateral dimensions of a cavity backreflector approach a point. As expected, the Q factor per unit length decreases with increasing thickness since diffraction from NP causes lateral spreading of the retro-reflecting light beyond the optical cross section of the resonant NP (see Supplemental Material [33], Fig. 4). The NRM field distribution [Fig. 4(f)] is similar to that from individual Au NPs, but resonant at 58° and nearly tenfold stronger than without the underlying Au mirror (see Supplemental Material [33], Fig. 5).

The NRMs depend on cavity thickness as for conventional Fabry-Perot modes, but experience far stronger plasmonic phase shifts due to multiple scattering, which needs to be taken into account. Plasmonically enhanced cross sections mean that, although dielectric nanoparticles also show NRMs, they are more than 50-fold weaker (Supplemental Material [33], Fig. 6). NRM modes are excited in all such plasmonic NP-dielectric microcavities, even with lower refractive indices (such as SiO_2 , see Supplemental Material [33], Fig. 7), thus demonstrating the universal nature of the modes in plasmonic-microcavity heterostructures.

These nanoresonator modes resemble the previously observed “Brewster mode,” but with the Bragg mirror replaced by flat Au and a NP. Such modes follow the condition [41,42]

$$E = \frac{hc^2}{2nL} \left(p + \frac{1}{2} \right) \cos(\theta), \quad (4)$$

where p is an integer, arising from additional π phase jumps compared to Fabry-Perot modes. Here, nanoresonator modes experience additional shifts of $\delta(E, \theta)$ dependent on the mirror, cavity, and nanoparticle compositions, with some analogy to Goos-Hänchen effects. This shifts the peaks considerably away from Eq. (4). As a result, these NRMs critically probe the morphology and scattering at the top interface.

Although our calculations yield good agreement with the mode energies, they do not account well for measured scattering intensities. Our model predicts that modes at

energies close to the transverse plasmon mode should have the greatest scattering intensity, but experimentally the modes at lower energies are much stronger. We suggest this may be due to additional Fano resonance [11,12] from the continuum scattering background [due to the slightly rough lower Au surface, gray line Fig. 2(b)], which is stronger at lower energies. Such Fano effects produce the asymmetric line-shape low-energy peaks and also the small (50 meV) extra blueshifts of the calculated modes [gray points, Fig. 2(b)] compared to those experimentally observed. It is also possible that the morphology of the nanoparticle favors out-coupling of cavity modes at lower energies.

In conclusion, we embed exfoliated hBN crystals in Au forming uniform planar half-microcavities. By depositing Au nanoparticles on top of these crystals to form NPoMC structures and using single nanoparticle spectroscopy, we probe plasmonic and Fabry-Perot enhancements, identifying interfacial scattering mechanisms that control redshifts in the mode positions. We identify a new microcavity nanoresonator mode that can be excited only for TM polarization at angles $\theta_B \pm 20^\circ$ and which depends on microcavity length and refractive index. We show that this mode arises from multiple reflections between scatterer and Au mirror. Subtle phase shifts and Fano coupling within this microcavity control its exact spectral position. These NRM modes are vital to understand when exploring the coupling of nanoparticles with the new materials landscape of TMDs. The same fabrication techniques can be used to produce NPoMC structures with other TMDs instead of hBN. This work is valuable in studying architectures (such as semiconductor and dielectric microcavities), which take advantage of enhancements at nanostructure or NPoMC interfaces. Moreover, due to the extreme sensitivity of these modes, they are suitable for exploring novel angle- and polarization-sensitive optical devices that are integrable and easy to fabricate.

This work is supported by EPSRC Grants No. EP/N016920/1, No. EP/L027151/1, No. EP/L016087/1, and No. NanoDTC EP/L015978/1, EU Horizon 2020 Grant No. 785219, the MEXT Element Strategy Initiative to Form Core Research Center, Grant No. JPMXP0112101001, CREST(JPMJCR15F3) JST. X.Z. acknowledges FWO Grants No. V420319N, No. K230919N, No. G090017N, and the KU Leuven internal funds C24/15/015, C14/19/083. O. S. O. acknowledges a Rubicon Fellowship from the Netherlands Organisation for Scientific Research and A. T. acknowledges Saint-Petersburg State University for a research Grant No. 51125686.

*jjb12@cam.ac.uk

- [1] C. Jin *et al.*, *Nat. Phys.* **13**, 127 (2017).
- [2] S. Latini, K. T. Winther, T. Olsen, and K. S. Thygesen, *Nano Lett.* **17**, 938 (2017).

- [3] G. H. Lee, Y. J. Yu, C. Lee, C. Dean, K. L. Shepard, P. Kim, and J. Hone, *Appl. Phys. Lett.* **99**, 243114 (2011).
- [4] S. Dai *et al.*, *Nat. Nanotechnol.* **10**, 682 (2015).
- [5] Q. Wang, J. Guo, Z. Ding, D. Qi, J. Jiang, Z. Wang, W. Chen, Y. Xiang, W. Zhang, and A. T. S. Wee, *Nano Lett.* **17**, 7593 (2017).
- [6] A. Kavokin, J. J. Baumberg, G. Malpuech, and F. P. Laussy, *Microcavities* (Oxford University Press, New York, 2017).
- [7] K. Vahala, *Nature (London)* **424**, 839 (2003).
- [8] X. Liu, T. Galfsky, Z. Sun, F. Xia, E.-c. Lin, Y.-H. Lee, S. Kéna-Cohen, and V. M. Menon, *Nat. Photonics* **9**, 30 (2015).
- [9] S. Dufferwiel *et al.*, *Nat. Commun.* **6**, 8579 (2015).
- [10] L. C. Flatten, Z. He, D. M. Coles, A. A. Trichet, A. W. Powell, R. A. Taylor, J. H. Warner, and J. M. Smith, *Sci. Rep.* **6**, 33134 (2016).
- [11] H. Y. Jeong *et al.*, *ACS Nano* **10**, 8192 (2016).
- [12] W. Wang, A. Klots, Y. Yang, W. Li, I. I. Kravchenko, D. P. Briggs, K. I. Bolotin, and J. Valentine, *Appl. Phys. Lett.* **106**, 181104 (2015).
- [13] M. E. Kleemann *et al.*, *Nat. Commun.* **8**, 1296 (2017).
- [14] J. Mertens *et al.*, *Nano Lett.* **13**, 5033 (2013).
- [15] D. O. Sigle *et al.*, *ACS Nano* **9**, 825 (2015).
- [16] T. Low, A. Chaves, J. D. Caldwell, A. Kumar, N. X. Fang, P. Avouris, T. F. Heinz, F. Guinea, L. Martin-Moreno, and F. Koppens, *Nat. Mater.* **16**, 182 (2017).
- [17] D. Zheng, S. Zhang, Q. Deng, M. Kang, P. Nordlander, and H. Xu, *Nano Lett.* **17**, 3809 (2017).
- [18] S. Butun, S. Tongay, and K. Aydin, *Nano Lett.* **15**, 2700 (2015).
- [19] S. Najmaei, A. Mlayah, A. Arbouet, C. Girard, J. Léotin, and J. Lou, *ACS Nano* **8**, 12682 (2014).
- [20] W. Liu, B. Lee, C. H. Naylor, H. S. Ee, J. Park, A. T. C. Johnson, and R. Agarwal, *Nano Lett.* **16**, 1262 (2016).
- [21] J. Wen *et al.*, *Nano Lett.* **17**, 4689 (2017).
- [22] N. Lundt *et al.*, *Nat. Commun.* **7**, 13328 (2016).
- [23] R. Chikkaraddy *et al.*, *ACS Photonics* **4**, 469 (2017).
- [24] X. Zheng, N. Verellen, V. Volskiy, V. K. Valev, J. J. Baumberg, G. A. E. Vandenbosch, and V. V. Moshchalkov, *Opt. Express* **21**, 31105 (2013).
- [25] C. Tserkezis, R. Esteban, D. O. Sigle, J. Mertens, L. O. Herrmann, J. J. Baumberg, and J. Aizpurua, *Phys. Rev. A* **92**, 053811 (2015).
- [26] F. Benz, B. de Nijs, C. Tserkezis, R. Chikkaraddy, D. O. Sigle, L. Pukenas, S. D. Evans, J. Aizpurua, and J. J. Baumberg, *Opt. Express* **23**, 33255 (2015).
- [27] M. E. Kleemann *et al.*, *ACS Nano* **11**, 850 (2017).
- [28] Z. Xi, Y. Lu, W. Yu, P. Yao, P. Wang, and H. Ming, *Opt. Lett.* **38**, 1591 (2013).
- [29] H. H. Anirban Mitra, S. Palomba, and L. Novotny, *Opt. Lett.* **35**, 953 (2010).
- [30] M. A. Schmidt, D. Y. Lei, L. Wondraczek, V. Nazabal, and S. A. Maier, *Nat. Commun.* **3**, 1108 (2012).
- [31] M. Bahramipanah, S. Dutta-Gupta, B. Abasahl, and O. J. Martin, *ACS Nano* **9**, 7621 (2015).
- [32] J. Li, M. Jiang, C. Xu, Y. Wang, Y. Lin, J. Lu, and Z. Shi, *Sci. Rep.* **5**, 9263 (2015).
- [33] See Supplemental Material at <http://link.aps.org/supplemental/10.1103/PhysRevLett.124.093901> for the fabrication method, all spectra individually plotted, results of simulations, and description of generalized Mie method, which includes Refs. [34–37].
- [34] J. Bruning and Y. Lo, *IEEE Trans. Antennas Propag.* **19**, 378 (1971).
- [35] D. M. Pozar, *Microwave Engineering* (John Wiley & Sons, New York, 2009).
- [36] R. C. Wittmann, *IEEE Trans. Antennas Propag.* **36**, 1078 (1988).
- [37] J. D. Jackson, *Classical Electrodynamics* (John Wiley & Sons, New York, 1999).
- [38] M. R. Hauwiller, L. B. Frechette, M. R. Jones, J. C. Ondry, G. M. Rotskoff, P. Geissler, and A. P. Alivisatos, *Nano Lett.* **18**, 5731 (2018).
- [39] T. Ishii and T. Sato, *J. Cryst. Growth* **61**, 689 (1983).
- [40] R. M. A. Azzam and N. M. Bashara, *Ellipsometry and Polarized Light* (North-Holland, Amsterdam, 1977).
- [41] H. F. Mahlein, *J. Opt. Soc. Am.* **64**, 647 (1974).
- [42] T. Taliercio, V. N. Guilengui, L. Cerutti, E. Tournié, and J.-J. Greffet, *Opt. Express* **22**, 24294 (2014).